Practicable model for phonon spectroscopy at atomic resolution in scanning transmission electron microscopy for thick crystalline specimens

Juri Barthel[1,*] and Leslie J. Allen[2,†]

[1]*Ernst Ruska-Centre (ER-C 2) Forschungszentrum Juelich GmbH, 52425 Juelich, Germany*

[2]*School of Physics, University of Melbourne, Parkville, Victoria 3010, Australia*

(Received 17 November 2024; revised 22 January 2025; accepted 18 February 2025; published 28 February 2025)

We generalize a recently proposed theory for atomic resolution phonon spectroscopy in scanning transmission electron microscopy, which explicitly includes the dependence of the spectrum on probe position, to apply to thick specimens, where probe channeling is important. We also take into account anisotropy due to atoms of the same species exhibiting different vibrational modes. This approach considers the contribution from individual atoms to the spectrum. Simulations to explore the dependence of the spectrum, in particular of its shape, on the probe position and thickness are carried out for the perovskite $SrTiO_3$, which has recently been experimentally investigated, and computational efficiency is discussed.

DOI: 10.1103/PhysRevB.111.054119

I. INTRODUCTION

The characterization of the vibrational states of materials at the atomic scale using electron energy-loss spectroscopy (EELS) in scanning transmission electron microscopy (STEM) has been made possible by advances in monochromation [1]. As pointed out in the recent review by Haas *et al.* [2], there have been relatively few demonstrations to date of the exploitation of a combination of atomic-scale spatial resolution and sub-10 meV energy resolution to observe variations in the vibrational EELS spectrum atom column by atom column, such as in Refs. [3–7]. Atomic resolution along one direction was also exploited to study vibrational modes at interfaces, e.g., in Refs. [8,9].

Several approaches, starting at the atomic level, have been employed to model the physics underlying the experimental results [5,10–25]. In this paper we will make comparisons with the frequency-resolved frozen phonon multislice (FRFPMS) method [21–23], first proposed by Zeiger and Rusz, in which the inelastic signal is computed as the difference between the incoherent and the coherent averages of exit wave functions computed over structure snapshots, considering only displacements due to vibrational modes within a narrow range of frequencies when calculating energy-loss spectra.

Another approach to simulating spectra, that explicitly includes the dependence on probe position in the inelastic scattering cross section itself and considers the contribution to the spectrum from individual atoms, was recently proposed by the present authors [25]. This approach allows for a change of shape in the spectrum as a function of probe position for specimens containing different atomic species, each making a specific contribution to the vibrational spectrum. As a demonstration of its utility, the approach was applied to the case of single-layer graphene containing Si and N impurities, and compared to experimental data obtained by Xu *et al.* [7], addressing single-atom vibrational spectroscopy with chemical-bonding sensitivity.

In the present paper we explicitly extend the theory developed in [25] to the case of thicker specimens, where channeling (multiple elastic scattering of the probing electrons) is important [23] and also to take into account anisotropy due to atoms of the same species exhibiting different vibrational modes in projection, the last point having recently been addressed in Refs. [26,27]. The anisotropy in the EELS signal arises due to the anisotropy of the vibrational modes of the material and due to the nonsymmetric collection geometry associated with an off-axis detector. Simulations to explore the dependence of the spectrum, in particular its shape, on the probe position and on specimen thickness are carried out for the perovskite $SrTiO_3$, which allows a comparison not only with the FRFPMS results in Ref. [26] but also with the high-quality experimental results presented there.

II. THEORY

We start with an expression for the contributions of single-phonon excitations to the intensity in the electron energy-loss spectrum measured in an off-axis detector D for the probe position $\mathbf{R}$; cf. Eq. (18) in Ref. [25]. In the single-phonon scattering approximation, the energy loss E is equal to the phonon energy. Taking the temperature dependence into account, the contribution from a slice i at depth z_i in the specimen reads as

*Contact author: ju.barthel@fz-juelich.de

†Contact author: lja@unimelb.edu.au

follows:

$$\frac{I(\mathbf{R}, z_i, E)}{dE} \approx \frac{h^2}{4Ek_0^2} \frac{e^{E/k_BT}}{e^{E/k_BT}-1} \sum_{\kappa} |\Psi_0(\mathbf{R}, z_i, \mathbf{R}_{i,\kappa})|^2 \times g^{i,\kappa}(E, \hat{\mathbf{q}}_D) \int_D \left[\tilde{f}_e^{i,\kappa}(\mathbf{q})\right]^2 q^2 \, d\mathbf{q}. \quad (1)$$

Here h is Planck's constant, k_0 is the wave number of the incident electron, k_B is Boltzmann's constant, and T is the temperature. The atoms in the slice i, enumerated by κ, are also assumed to contribute independently and with a weighting given by the intensity of the probe $|\Psi_0(\mathbf{R}, z_i, \mathbf{R}_{i,\kappa})|^2$ at the atomic position $\mathbf{R}_{i,\kappa}$. The elastic wave function $\Psi_0(\mathbf{R}, z_i, \mathbf{r})$ in the slice plane at z_i for a given incident probe position $\mathbf{R}$ can be obtained by multislice calculations that include channeling effects due to multiple scattering [28]. The term

$$g^{i,\kappa}(E, \hat{\mathbf{q}}_D) = \sum_{j'} \delta(E - E_{j'}) \left(\hat{\mathbf{q}}_D \cdot \boldsymbol{\varepsilon}_{j'}^{i,\kappa}\right)^2 \quad (2)$$

is the phonon density of states (PDOS) projected onto the atom κ in slice i along the direction of the unit vector $\hat{\mathbf{q}}_D$, where the sum is over vibrational modes j' with energies $E_{j'}$ and polarization vectors $\boldsymbol{\varepsilon}_{j'}^{i,\kappa}$ for the atoms. In Eq. (2), the dependence on the direction of projection of the PDOS $g^{i,\kappa}(E, \hat{\mathbf{q}}_D)$ is given by the unit vector $\hat{\mathbf{q}}_D = \mathbf{q}_D/|\mathbf{q}_D|$, with $\mathbf{q}_D = \int_D \mathbf{q} \, d\mathbf{q}$, where the integration is over all scattering vectors $\mathbf{q}$ into the detector D and, in contrast to Eq. (18) in Ref. [25], isotropy is not assumed here. We do not indicate this directional dependence explicitly on the left-hand side of Eq. (1), as it is a fixed parameter of the off-axis detector setup and this also keeps the notation more compact. The final term in Eq. (1) also involves integration up over all $\mathbf{q}$ into the off-axis detector D. The function $\tilde{f}_e^{i,\kappa}(\mathbf{q})$ is given by

$$\tilde{f}_e^{i,\kappa}(\mathbf{q}) = f_e^{i,\kappa}(\mathbf{q}) \exp\left(-2\pi^2 \mathbf{q}^T \mathbf{U}_T^{i,\kappa} \mathbf{q}\right)/\sqrt{m_{i,\kappa}}, \quad (3)$$

with $f_e^{i,\kappa}(\mathbf{q})$ the electron scattering factor and $m_{i,\kappa}$ the mass of atom κ in the slice at z_i. In this formulation, the exponential Debye-Waller factor depends on anisotropic mean-squared displacements (MSDs) described by the components of the matrix $\mathbf{U}_T^{i,\kappa}$ [29]. The diagonal components $U_{T,jj}^{i,\kappa}$ with $j \in \{1, 2, 3\}$ correspond to the MSDs along one of the three spatial dimension for a particular temperature, denoted by the subscript T. Off-diagonal terms are zero in our calculations.

It is useful to write Eq. (1) in the form

$$\frac{I(\mathbf{R}, z_i, E)}{dE} = F_T(E) \sum_{\kappa} \alpha^{i,\kappa}(\mathbf{R}) \, g^{i,\kappa}(E, \hat{\mathbf{q}}_D), \quad (4)$$

where

$$F_T(E) = \frac{h^2}{4Ek_0^2} \frac{\exp(E/k_BT)}{\exp(E/k_BT)-1} \quad (5)$$

and

$$\alpha^{i,\kappa}(\mathbf{R}) = |\Psi_0(\mathbf{R}, z_i, \mathbf{R}_{i,\kappa})|^2 \int_D \left[\tilde{f}_e^{i,\kappa}(\mathbf{q})\right]^2 q^2 \, d\mathbf{q}. \quad (6)$$

Note that Eq. (5) has a different energy dependence for simulating energy gain [24]. In the summation over κ in Eq. (4), some of the atoms of the same type (isotopes) may have a similar projected PDOS. We label such a set as $\tau_{i,n}$ and refer to the subscript n as a class of atoms. Then Eq. (4) may be rewritten as

$$\frac{I(\mathbf{R}, z_i, E)}{dE} = F_T(E) \sum_{n} \sum_{\kappa \in \tau_{i,n}} \alpha^{i,\kappa}(\mathbf{R}) \, g^{i,\kappa}(E, \hat{\mathbf{q}}_D). \quad (7)$$

The above definition of classes as sets of atoms of the same type and the same projected PDOS is not specific for a particular slice of a thick specimen. This allows us to relabel the projected PDOS as $g_n(E, \hat{\mathbf{q}}_D)$ and factor out the PDOS shared by all atoms of one class when accumulating the contributions from all slices. This last step is possible due to the assumption that the effect of further elastic scattering after the inelastic scattering event is the same, irrespective of the slice in which the transition occurs. This is reasonable to assume for an EELS detector with a sufficiently large acceptance angle [30]. Swapping the sequence of summation, we obtain the expression

$$\frac{I(\mathbf{R}, E)}{dE} = \sum_i \frac{I(\mathbf{R}, z_i, E)}{dE} = F_T(E) \sum_n \alpha_n(\mathbf{R}) \, g_n(E, \hat{\mathbf{q}}_D) \quad (8)$$

for the accumulated EELS signal into the off-axis detector, where

$$\alpha_n(\mathbf{R}) = \sum_i \sum_{\kappa \in \tau_{i,n}} \alpha^{i,\kappa}(\mathbf{R}). \quad (9)$$

Calculations using this sequence of summations are efficient for (while not being limited to) periodic structures since the number of classes is usually much lower than the number of slices for a thick crystal. In the case of defects or interface structures with reduced periodicity, many classes containing just one or a few atoms are required. The original summation sequence in Eq. (4) may then be more computationally efficient in terms of memory consumption. The form of Eq. (8) allows us to separate out the contributions of each class of atoms to the energy-loss spectrum and investigate how they vary as a function of probe position, specimen thickness, and other experimental parameters.

The factor $F_T(E)$ in Eq. (8), as given by Eq. (5), modulates the shape of the energy-loss spectrum relative to the shape of the PDOS and, in general, intensities at low energy losses are amplified. The quantity

$$s_{n,T}(E, \hat{\mathbf{q}}_D) = F_T(E) \, g_n(E, \hat{\mathbf{q}}_D), \quad (10)$$

represents the *spectral contribution* for each class n and determines the dependence on energy loss E. The dependence on probe position $\mathbf{R}$ and specimen thickness, due to variations in channeling, is given by the respective weighting function $\alpha_n(\mathbf{R})$, wherein the dependence on specimen thickness is implicit in the sum over slices i in Eq. (9). Therefore, since the atoms contribute incoherently, we will refer to the approach presented here as the *channeling incoherent spectral contributions* (CHISCO) model in what follows.

III. EXAMPLE

Now let us demonstrate the application of Eq. (8) for simulations of STEM EELS that explore the dependence of the

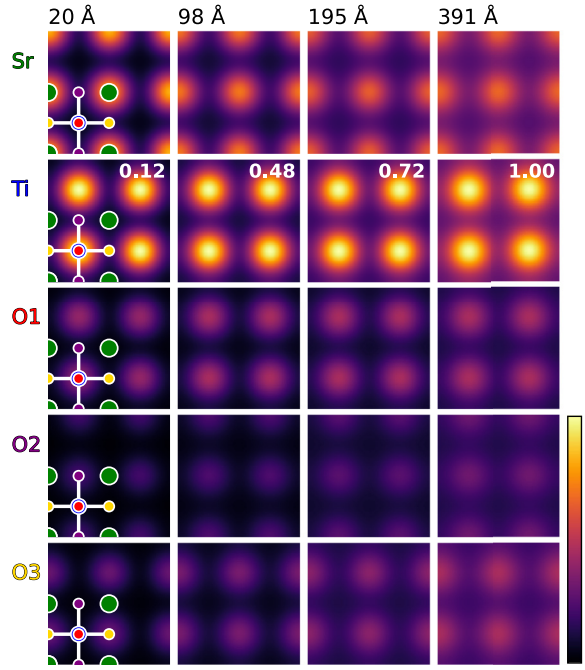

FIG. 1. Weighting functions $\alpha_n(\mathbf{R})$ for $n =$ Sr, Ti, O1, O2, and O3 in $SrTiO_3$ crystals of different thickness in [001] orientation. The maps correspond to scans over 2×2 projected unit cells and the projected structure of a unit cell is shown on the leftmost panels. The atomic columns on the corners of the unit cell contain Sr atoms (green). The column at the center of the unit cell contains Ti atoms (blue) and O1 type oxygen atoms (red) with an out-of-plane bond. Halfway between the Sr columns there are either pure O2 atomic columns (purple) at bottom and top or pure O3 columns (orange) on the left and right. White lines indicate the in-plane Ti-O2 and Ti-O3 bonds. Maps in each column are for the same specimen thickness, noted above, and share the same color scaling. In the linear color scale, black is at a value of $\alpha_n(\mathbf{R}) = 0$ and the brightest color (yellow) is at the maximum value for each thickness. Numbers given in the Ti maps show the relative maximum intensity as a function of thickness.

energy-loss spectrum on probe position and specimen thickness. We apply conditions similar to those used in Ref. [26], where experimental data were taken for a 50 unit cell thick specimen of $SrTiO_3$ in the [001] orientation with the aim of investigating frequency-dependent vibrational anisotropies in a centrosymmetric crystalline lattice. We assume incident electrons with a kinetic energy of 60 keV and a probe forming aperture defining a semiconvergence angle of 33 mrad. The EELS detector has an aperture of 25 mrad and is centered 62 mrad off axis. In Ref. [26] one set of measurements had the detector off axis along the [100] crystal direction and a second data set was obtained with the detector offset along the [010] direction. For our purposes it suffices to consider only one of these, and we choose the first case here, i.e., the offset along the [100] direction, which is along the horizontal axis in the relevant two-dimensional plots that follow. A finite source size with a FWHM of 2 Å is included in the calculations to take into account limitations on the spatial resolution of the experimental results.

TABLE I. Atomic mean-squared displacements (MSDs) of $SrTiO_3$ in $Å^2$ units at around $T = 300$ K from calculations and experiment. Isotropic MSDs (iso) are given for all atom types, and directional MSDs are given for O atoms parallel (∥) and perpendicular (⊥) to the Ti-O bond. More detail is in the text.

MSD	MD traj. [26]	PDOS [26]	X-rays [31]
$\langle u_T^2 \rangle_{\mathrm{Sr}}^{\mathrm{iso}}$	0.00690	0.00572	0.00785
$\langle u_T^2 \rangle_{\mathrm{Ti}}^{\mathrm{iso}}$	0.00373	0.00313	0.00556
$\langle u_T^2 \rangle_{\mathrm{O}}^{\parallel}$		0.00282	0.00463
$\langle u_T^2 \rangle_{\mathrm{O}}^{\perp}$		0.01203	0.01205
$\langle u_T^2 \rangle_{\mathrm{O}}^{\mathrm{iso}}$	0.00850	0.00896	0.00958

Figure 1 shows weighting functions $\alpha_n(\mathbf{R})$, as given by Eq. (9), for $n =$ Sr, Ti, and three classes of O atoms for different specimen thicknesses. The three classes of O atoms arise not only due to their differences in position but also in the projection of bonding to the adjacent Sr and Ti atoms. This can be understood from the insets in the leftmost panels of Fig. 1, which show the projected structure of one $SrTiO_3$ unit cell. For each O atom, the vibrational properties are different parallel to the Ti-O bond compared to the two perpendicular directions [26,31]. In the present scenario, with the detector off-axis position along the horizontal direction, O1 and O2 share the same projected PDOS because, for those atoms, the projection of the PDOS along $\hat{\mathbf{q}}_D$, which is horizontal, takes the components of all vibrational modes perpendicular to the bond, while O3 has a different projected PDOS determined by the components of the vibrational modes parallel to the bond. This is also reflected by different directional MSDs as listed in Table I. Specifically, the pertinent components of the matrix $\mathbf{U}_T^{i,\kappa}$ in Eq. (3), for an in-plane $\mathbf{q}$, are $U_{T,22}^{i,\mathrm{O2}} = U_{T,11}^{i,\mathrm{O3}} = \langle u_T^2 \rangle_{\mathrm{O}}^{\parallel}$ and $U_{T,11}^{i,\mathrm{O1}} = U_{T,22}^{i,\mathrm{O1}} = U_{T,11}^{i,\mathrm{O2}} = U_{T,22}^{i,\mathrm{O3}} = \langle u_T^2 \rangle_{\mathrm{O}}^{\perp}$ in any atomic plane at z_i where these atoms are located and with $U_{T,12}^{i,\kappa} = U_{T,21}^{i,\kappa} = 0$ for all atoms in the structure. The MSDs for Sr and Ti atoms are isotropic.

For the calculation of weighting functions $\alpha_n(\mathbf{R})$ we applied anisotropic MSDs via the matrix $\mathbf{U}_T^{i,\kappa}$ in Eq. (3) and also within the quantum excitation of phonons (QEP) model [12,14] to calculate the elastic probe intensities $|\Psi_0(\mathbf{R}, z_i, \mathbf{R}_{i,\kappa})|^2$ used in Eq. (6) via the multislice algorithm [32]. Yan *et al.* [26] used isotropic Debye-Waller factors based on isotropic MSDs, the values listed in the left-most column of Table I, which were calculated directly from the trajectories obtained using molecular dynamics (MD). In our simulations, we applied the MSDs listed in the rightmost column of Table I, which were obtained from x-ray diffraction data at $T = 296$ K by Abramov *et al.* [31] for electron scattering factors of neutral atoms (also used here). These and very similar MSDs have been successfully applied (albeit in an isotropic approximation) to provide excellent quantitative fits between simulations and experiments in high-resolution STEM and TEM imaging [33,34]. It should be noted that MSDs applied in these two investigations were calculated by Peng [35] by averaging the two sets of values obtained by Abramov *et al.* [31] for atomic

and ionic scattering factors. We note, in passing, that an incorrect reference was mistakenly given in Ref. [33] for the source of the MSDs used there. In the middle column of Table I we also list MSDs that we calculated from the projected PDOSs provided in Ref. [26] for $T = 300$ K using the formula

$$\langle u_T^2 \rangle_n = \frac{\hbar^2}{2m_n} \int_0^{E_m} \coth\left(\frac{E}{2k_B T}\right) \frac{g_n(E)}{E}\, dE. \qquad (11)$$

The MSDs obtained in this way are lower than those calculated from MD trajectories, an inconsistency that is yet to be accounted for. Furthermore, both sets of MSDs associated with Ref. [26] are lower than those consistent with x-ray diffraction [31] and, as just discussed, used successfully in quantitative microscopy.

A supercell of $12 \times 12 \times 1$ unit cells was used in accumulating the $\alpha_n(\mathbf{R})$ as a function of specimen thickness. The supercell was partitioned into two slices of ≈2 Å thickness along [001], the incident probe direction, and the projected potentials were sampled on a grid of 576×576 pixels. Atomic scattering factors for electrons, as tabulated by Weickenmeier and Kohl [36], were used to calculate 400 projected potentials for random configurations of the atoms in each slice consistent with the MSDs in the rightmost column of Table I. An Einstein model was assumed, i.e., the thermal displacements of individual atoms were uncorrelated. These sets of projected potentials were stacked in random permutations out to a specimen thickness of 391 Å (100 unit cells). The distributions of the elastic probe intensity $|\Psi_0(\mathbf{R}, z_i, \mathbf{r})|^2$, as the probe was propagated through each atomic plane z_i, were obtained by coherently averaging over repeated multislice passes, as usually done in the QEP model [12]. In order to ensure convergence of the elastic probe images, the multislice passes were repeated 600 times for each probe position, each time with a random selection of stacked projected potentials. The calculations were performed for a set of 12×12 probe positions $\mathbf{R}$, uniformly spaced over one projected unit cell (satisfying the Nyquist sampling requirement). The calculations were carried out with the DR. PROBE software [37]. The subsequent accumulation of the $\alpha_n(\mathbf{R})$ as a function of probe position, specimen thickness, and atom class from the elastic probe images and the atomic structure model of $SrTiO_3$ was performed using PYTHON scripts.

It is clear in Fig. 1 that the relative contributions from each class of atoms change as a function of thickness. In particular, the contributions for O atoms become more prominent as the thickness increases. The maps for each class of atoms are clearly peaked at the respective atomic positions, and the weights for the Ti contribution reach the highest value for all thicknesses. The Sr atoms are the strongest scatterers in this compound. However, the (elastically scattered) electron probe stays more tightly bound to the Ti-O1 column. With increasing specimen thickness, all maps build up a nonzero background, which means that each class also contributes to the spectrum for probe positions that are away from the projected atomic sites. In addition, the weights increase overall as a function of thickness, as indicated by the numbers given in the Ti maps, which express the maximum in each column as a fraction of that at 391 Å thickness.

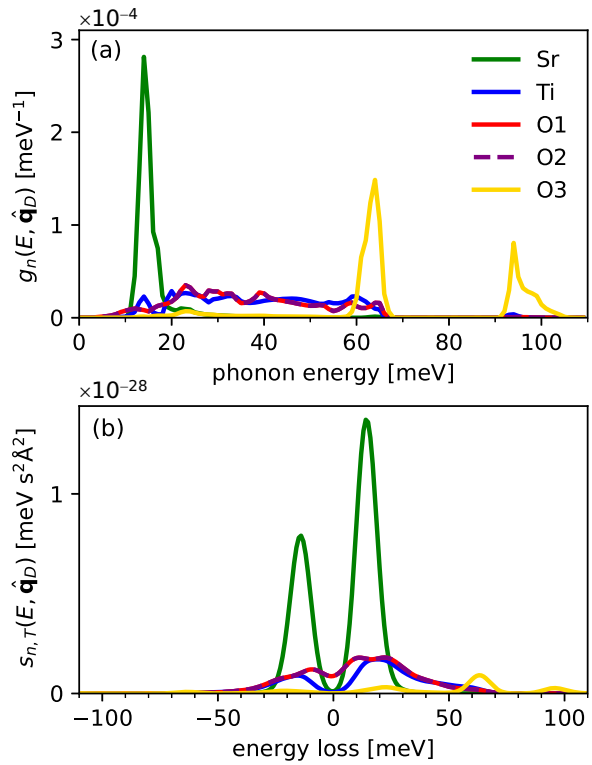

FIG. 2. (a) Projected PDOS for each atom class n in $SrTiO_3$, reproduced from Figs. 1 and 3 in Ref. [26] and normalized such that the area under each curve is 1. The projection is for an off-axis position of the EELS detector along the [100] direction. (b) Spectral contribution of each class n calculated from the projected PDOSs in (a) for an incident beam energy of 60 keV and at a specimen temperature of $T = 300$ K. The functions are smoothed by a Gaussian of 10 meV FWHM to simulate the limited energy resolution of the spectrometer.

To calculate energy loss spectra from the weighting factors $\alpha_n(\mathbf{R})$ via Eq. (8) one requires PDOSs $g_n(E, \hat{\mathbf{q}}_D)$ projected onto the different atom classes n. We used the projected PDOSs calculated in Ref. [26]. However, here they have been smoothed over an energy window of 1 meV and then normalized such that their integration over phonon energy is unity, as shown in Fig. 2(a). As noted before, for the off-axis detector position along the horizontal direction in Fig. 1, the projected directional PDOSs for O1 and O2 atoms are equal and determined by the vibrational modes perpendicular to their respective bond with the Ti atoms. In contrast, the O3 PDOS is different and determined by the vibrational modes parallel to the bond. These PDOSs have been used to calculate spectral contributions by applying Eq. (10) for each class n of atoms shown in Fig. 2(b), assuming an incident beam energy of 60 keV and a specimen temperature $T = 300$ K. The negative part of the energy-loss axis corresponds to energy gain of the probing electron. In addition, the spectral contributions are smoothed by a Gaussian of 10 meV FWHM to simulate the limitations on energy resolution in the experiment [26].

In Fig. 3 we show phonon EELS maps for 60 keV electrons incident on $SrTiO_3$ with the detector off axis along the horizontal [100] direction by 62 mrad. In Fig. 3(a) experimental, background-subtracted EELS maps are reproduced from

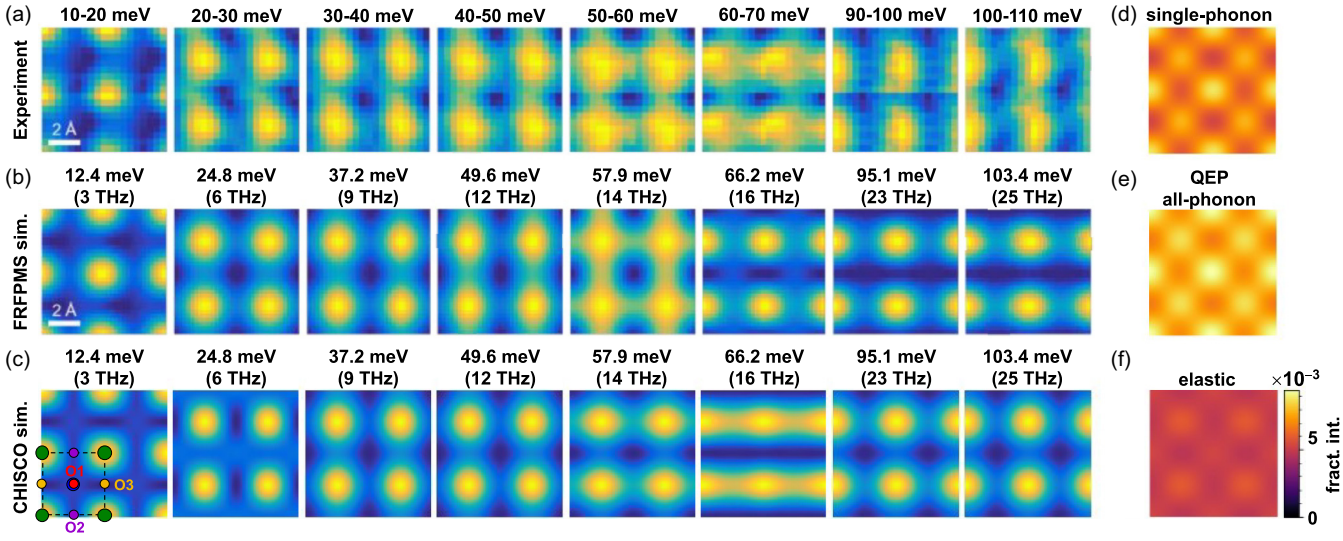

FIG. 3. EELS maps for $SrTiO_3$ in [001] orientation with the detector off axis along the horizontal [100] direction by 62 mrad. (a) Experimental EELS maps (after background subtraction) for the set of energy-loss ranges indicated above each map. These are reproduced from Fig. 2(e) in Ref. [26]. (b) Maps simulated using the FRFPMS model integrating over a window of ±0.5 THz (≈ ±2 meV) about the representative energy losses indicated. These are reproduced from Fig. 2(f) in Ref. [26]. (c) Simulations using the CHISCO model in this paper for bins centered as indicated in (b) and with a range of ±2 meV. (d) Single phonon integrated EELS map. Intensity scattered into the off-axis detector (e) due to phonon excitation and (f) for elastically scattered electrons, both calculated in the QEP model. (d), (e), and (f) are plotted on the same intensity scale in fractions of the incident beam intensity.

Fig. 2(e) in Ref. [26]. The simulations from Ref. [26] that were calculated with the FRFPMS approach for comparison with these experimental results are reproduced in Fig. 3(b). These maps take into account single-phonon excitations and were integrated over bins centered as indicated and with a range of ±0.5 THz (≈±2 meV). In Fig. 3(c) we show results from simulations using the CHISCO model discussed in this paper and integrated over the same energy bins used in Fig. 3(b). The two theoretical approaches mostly agree, with notable differences in the scan patterns around 14 and 16 THz. Although the patterns are peaked at the same probe positions, they differ slightly between the peaks. Around 14 THz, the FRFPMS calculation predicts higher intensity at O2 and O3 column positions than the CHISCO calculation, and is more consistent with experiment. Around 16 THz, the CHISCO result predicts higher intensity at Ti-O1 positions, producing horizontal stripe features similar to the experimental pattern. For the patterns at 23 and 25 THz, the CHISCO result predicts noticeably more intensity than the FRFPMS calculation at Sr positions, also arguably in somewhat better agreement with the experiment.

In Fig. 3(d) we show the integrated intensity obtained by summing the theoretical calculations in Fig. 3(c) together with further maps covering the complete range of energy losses and gains to include all single-phonon contributions to the spectrum. This integrated result is depicted using the color scale shown to the right of Fig. 3(f), which now provides an absolute scale as a fraction of the incident beam intensity. We note that patterns for energy losses and gains taken symmetrically around the zero loss are similar up to a Boltzmann factor, i.e., they do look similar if each is plotted on its own scale.

For comparison, we show the result of calculations in the QEP model in Fig. 3(e) on the same scale. Single-phonon and multi-phonon excitations as well as multiple inelastic scattering, which is becoming important for a specimen that is 200 Å thick [33], are implicit in these calculations. These results are rather similar in pattern with maxima at the Sr column position. As expected, the QEP calculation predicts larger inelastic scattering intensity, because it includes the single-phonon excitations as one component.

With the detector placed just outside the bright field, there is also a significant elastic intensity scattered into the off-axis detector. According to our calculations using the QEP model, as shown in Fig. 3(f), the intensity scattered elastically into the off-axis detector is only slightly smaller than that due to phonon excitations and produces a pattern that is peaked at the Ti-O1 column positions. Since $SrTiO_3$ has ionic character, this suggests that electrons scattered elastically in the direction of the detector and subsequently scattered through small angles may contribute a dipole contribution. However, dipole inelastic scattering components were not included in this calculation.

Let us now take a more specific and detailed look at simulated energy-loss spectra, some implicit in Fig. 3. Figure 4(a) shows energy-loss spectra for four specific probe positions covered by the maps in Fig. 3. There is a strong shape dependence in the spectra when the probe is placed above the four different atomic columns. What is clearly seen in 4(a) is the change of shape of the spectrum and not just the variation in intensity. In Fig. 4(b) we explore the changes in shape of the spectrum for thicknesses considerably thinner and thicker than that for the experimental data in Ref. [26], with only subtle variations in shape being evident in this example with the probe placed on the Ti-O1 column. Figure 4(c) illustrates the utility of the formalism presented here to explore the relative contributions from different classes of atoms. The example

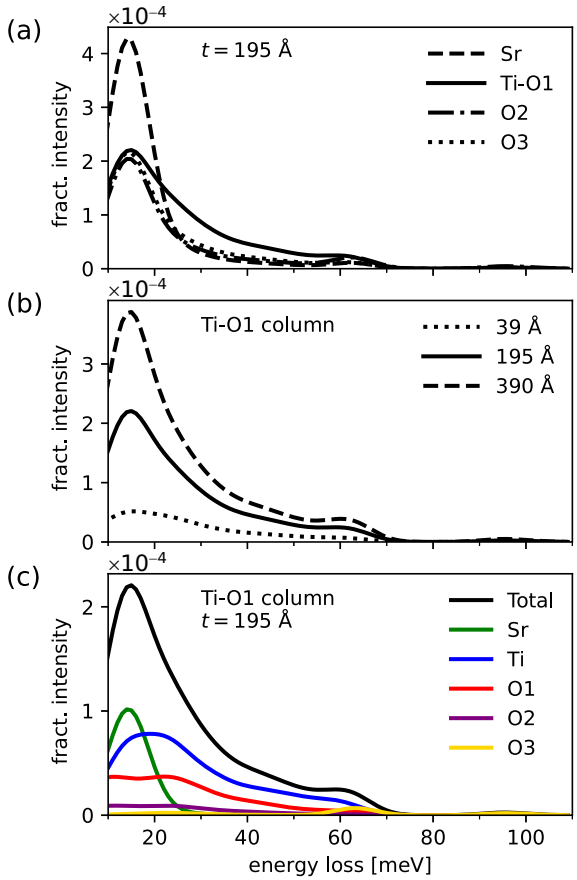

FIG. 4. Simulated energy-loss spectra (a) with the electron probe placed over the four different atomic columns of a 195 Å thick $SrTiO_3$ crystal in [001] orientation, (b) for different specimen thicknesses and the probe placed over a Ti-O1 column, and (c) contributions to the spectrum for each class of atoms with the probe placed over a Ti-O1 column and at 195 Å thickness. Spectrometer energy-loss bins of 1 meV width are assumed for the calculation of fractional intensities.

shows that the spectrum for the probe placed over a Ti-O1 column of 195 Å thick $SrTiO_3$ has contributions from all classes of atoms, each with its particular energy dependence. That all classes contribute to such a spectrum and that the shape of the spectrum shows only subtle changes as a function of thickness, as noted in Fig. 4(b), are mostly due to the relatively large source size assumed here (2 Å FWHM).

IV. DISCUSSION AND CONCLUSIONS

In this paper, we have extended a recently proposed theory for atomic resolution phonon spectroscopy in STEM to the case of thicker crystalline specimens. This formulation explicitly includes the dependence of the spectrum on probe position and considers the contributions to the spectrum from individual atoms. Simulations to explore the thickness dependence of the energy-loss spectra, in particular their shape, are carried out for the perovskite $SrTiO_3$. The calculations are compared qualitatively to results of a recent experimental investigation and to calculations using the FRFPMS approach [26,27].

We reiterate two key assumptions made. We have an EELS detector accepting a large range of scattering angles and placed sufficiently far off axis in the dark field that we can assume incoherent contributions from different atoms [25]. In this model we do not explicitly consider the details of phonon modes in the dispersion surfaces, and a PDOS projected onto each atom is assumed to be sufficient. Nevertheless, unlike in Ref. [25] where the probe could be assumed, roughly speaking, to be illuminating only one atom at a time, here probe spreading means that several atoms may be illuminated at a given slice. In this scenario, the cross-terms between atoms due to correlated vibration of the atoms *may* be significant. Nevertheless, the broad qualitative agreement with the FRFPMS model and experiment shown in Fig. 3 suggests that the approximation of incoherent contributions from different atoms is a reasonable one. It is likely that the large probe convergence angle and large detector aperture used here lead to a suppression of any contributions from cross-terms between atoms.

Working in this incoherent approximation, where atoms contribute independently, makes calculations inherently faster than methods where this is not assumed [20,21]. The calculation of the multiple elastic electron scattering in a thick specimen (or for a range of thicknesses) and for a set of probe positions, as in the present example, is a matter of a few hours on a contemporary desktop computer, including postprocessing into weighting functions $\alpha_n(\mathbf{R})$ for each class of atoms. The main contribution to the computation time is the large number of multislice calculations within the QEP model, which are repeated several hundred times per probe position with different positional configurations of the atoms to achieve convergence for the calculation of elastically scattered probe intensity distributions. A significant reduction of computational cost (times down to a few minutes) could be achieved by applying absorptive potentials for which just one multislice calculation is sufficient per probe position. While absorptive form factors for electron scattering are usually available considering MSDs in an isotropic approximation [36], they could also be obtained for anisotropic MSDs as proposed by Peng [35].

A prerequisite to apply the CHISCO approach is that projected PDOSs are available for each class of atoms. Ideally these would provide consistent MSDs to be used in multislice calculations and in Eq. (6), and also to calculate spectral contributions $s_{n,T}(E, \hat{\mathbf{q}}_D)$ as input to the calculation of the energy-loss spectra. In the discussion of Table I, we noted that the MSDs deduced from MD trajectories by Yan *et al.* [26] are (i) inconsistent with the MSDs that we have calculated via Eq. (11) from the projected PDOS, and (ii) they are also significantly smaller than those determined by Abramov *et al.* from x-ray scattering experiments [31]. A possible contribution to the first inconsistency is that Eq. (11) applies properties of quantum harmonic oscillators, while the MSDs are determined from MD calculations that numerically solve classical equations of motion. Concerning the second inconsistency with the results of Abramov *et al.*, we found that using the smaller MSDs, which are consistent with the PDOSs, leads to an increased inelastic scattering intensity in the CHISCO model, due to larger Debye-Waller factors in Eq. (3), and at the same time reduces the total thermal diffuse

scattering estimated by the QEP model. These two changes were so strong that the single-phonon scattering estimated by the CHISCO method became larger than the QEP result, which should contain single-phonon excitations as one of its components. As shown in Figs. 3(d) and 3(e), this problem is not present when using the MSDs determined by Abramov *et al.*. The success of quantitative high-resolution STEM and TEM imaging using these MSDs suggests that they could be more realistic, a topic which is worth revisiting.

The approach discussed here can simulate the main features of energy-loss spectra measured in STEM using an off-axis detector, given suitable projected PDOSs. How the electron probe channels through the crystal has a nontrivial effect on the shape of the energy-loss spectrum. Our simulations for the example of $SrTiO_3$ suggest that the change of shape of the spectrum occurs mostly as a function of probe position and to a lesser extent as a function of thickness. Contributions to the spectrum from different classes of atoms can be explored, a feature that is not available with other approaches. A further advantage of the CHISCO approach is that the simulations have modest computational requirements and this allows one to explore the parameter space with the aim of optimizing the experimental setup for the investigation of a particular specimen of interest.

As previously discussed [25], deconvolution of the multiple scattering of the probe to obtain projected PDOSs per atom is possible in principle, in a similar way to how this was done for core-loss EELS [38], albeit that the atomic positions and the mean-squared displacements would need to be known *a priori* for each atom in the specimen. The results shown in Fig. 4(c) indicate that, for phonon EELS of a thick compound specimen, a spectrum is in general a weighted superposition of contributions from different atom classes. This suggests that further investigation is warranted to determine whether the signal of localized phonon modes occurring for impurity atoms and at interfaces can be measured by such a deconvolution approach. As a result of such an analysis, it should be possible to extract the projected PDOS for a given class of atoms by inversion of the set of linear equations given by Eq. (8) from energy-loss spectra taken as a function of probe position. Assuming that the atomic structure is known, the quantities $F_T(E)$ and $\alpha_n(\mathbf{R})$ can be calculated and the projected PDOS $g_n(E, \hat{\mathbf{q}}_D)$ at each E and for each class of atoms n can be obtained by solving a set of linear equations. This opens up a new experimental pathway to explore the vibrational behavior of individual atoms.

ACKNOWLEDGMENTS

We acknowledge helpful discussions with Ján Rusz, corresponding author on the arXiv submission Ref. [26], and we are grateful to him for permission to use material contained therein, as detailed in the text. We also thank all the other authors of Ref. [26].

[1] O. L. Krivanek, T. C. Lovejoy, N. Dellby, T. Aoki, R. W. Carpenter, P. Rez, E. Soignard, J. Zhu, P. E. Batson, M. J. Lagos, R. F. Egerton, and P. A. Crozier, Vibrational spectroscopy in the electron microscope, Nature (London) **514**, 209 (2014).

[2] B. Haas, C. T. Koch, and P. Rez, Perspective on atomic-resolution vibrational electron energy-loss spectroscopy, Appl. Phys. Lett. **125**, 150502 (2024).

[3] F. S. Hage, D. M. Kepaptsoglou, Q. M. Ramasse, and L. J. Allen, Phonon spectroscopy at atomic resolution, Phys. Rev. Lett. **122**, 016103 (2019).

[4] K. Venkatraman, B. D. Levin, K. March, P. Rez, and P. A. Crozier, Vibrational spectroscopy at atomic resolution with electron impact scattering, Nat. Phys. **15**, 1237 (2019).

[5] F. S. Hage, G. Radtke, D. M. Kepaptsoglou, M. Lazzeri, and Q. M. Ramasse, Single-atom vibrational spectroscopy in the scanning transmission electron microscope, Science **367**, 1124 (2020).

[6] B. Haas, T. M. Boland, C. Elsässer, A. K. Singh, K. March, J. Barthel, C. T. Koch, and P. Rez, Atomic-resolution mapping of localized phonon modes at grain boundaries, Nano Lett. **23**, 5975 (2023).

[7] M. Xu, D.-L. Bao, A. Li, M. Gao, D. Meng, A. Li, S. Du, G. Su, S. J. Pennycook, S. T. Pantelides, and W. Zhou, Single-atom vibrational spectroscopy with chemical-bonding sensitivity, Nat. Mater. **22**, 612 (2023).

[8] Y.-H. Li, R.-S. Qi, R.-C. Shi, J.-N. Hu, Z.-T. Liu, Y.-W. Sun, M.-Q. Li, N. Li, C.-L. Song, L. Wang, Z.-B. Hao, Y. Luo, Q.-K. Xue, X.-C. Ma, and P. Gao, Atomic-scale probing of heterointerface phonon bridges in nitride semiconductor, Proc. Natl. Acad. Sci. USA **119**, e2117027119 (2022).

[9] T. Lee, J. Qi, C. A. Gadre, H. Huyan, S.-T. Ko, Y. Zuo, C. Du, J. Li, T. Aoki, R. Wu *et al.*, Atomic-scale origin of the low grain-boundary resistance in perovskite solid electrolyte $Li_{0.375}Sr_{0.4375}Ta_{0.75}Zr_{0.25}O_3$, Nat. Commun. **14**, 1940 (2023).

[10] A. Amali and P. Rez, Theory of lattice resolution in high-angle annular dark-field images, Microsc. Microanal. **3**, 28 (1997).

[11] A. V. Martin, S. D. Findlay, and L. J. Allen, Model of phonon excitation by fast electrons in a crystal with correlated atomic motion, Phys. Rev. B **80**, 024308 (2009).

[12] B. D. Forbes, A. V. Martin, S. D. Findlay, A. J. D'Alfonso, and L. J. Allen, Quantum mechanical model for phonon excitation in electron diffraction and imaging using a Born-Oppenheimer approximation, Phys. Rev. B **82**, 104103 (2010).

[13] N. R. Lugg, B. D. Forbes, S. D. Findlay, and L. J. Allen, Atomic resolution imaging using electron energy-loss phonon spectroscopy, Phys. Rev. B **91**, 144108 (2015).

[14] B. D. Forbes and L. J. Allen, Modeling energy-loss spectra due to phonon excitation, Phys. Rev. B **94**, 014110 (2016).

[15] C. Dwyer, T. Aoki, P. Rez, S. L. Y. Chang, T. C. Lovejoy, and O. L. Krivanek, Electron-beam mapping of vibrational modes with nanometer spatial resolution, Phys. Rev. Lett. **117**, 256101 (2016).

[16] C. Dwyer, Prospects of spatial resolution in vibrational electron energy loss spectroscopy: Implications of dipolar scattering, Phys. Rev. B **96**, 224102 (2017).

[17] L. J. Allen, H. G. Brown, S. D. Findlay, and B. D. Forbes, A quantum mechanical exploration of phonon energy-loss

spectroscopy using electrons in the aloof beam geometry, Microscopy **67**, i24 (2018).

[18] R. J. Nicholls, F. S. Hage, D. G. McCulloch, Q. M. Ramasse, K. Refson, and J. R. Yates, Theory of momentum-resolved phonon spectroscopy in the electron microscope, Phys. Rev. B **99**, 094105 (2019).

[19] R. Senga, K. Suenaga, P. Barone, S. Morishita, F. Mauri, and T. Pichler, Position and momentum mapping of vibrations in graphene nanostructures, Nature (London) **573**, 247 (2019).

[20] P. Rez and A. Singh, Lattice resolution of vibrational modes in the electron microscope, Ultramicroscopy **220**, 113162 (2021).

[21] P. M. Zeiger and J. Rusz, Efficient and versatile model for vibrational STEM-EELS, Phys. Rev. Lett. **124**, 025501 (2020).

[22] P. M. Zeiger and J. Rusz, Frequency-resolved frozen phonon multislice method and its application to vibrational electron energy loss spectroscopy using parallel illumination, Phys. Rev. B **104**, 104301 (2021).

[23] P. M. Zeiger, J. Barthel, L. J. Allen, and J. Rusz, Lessons from the harmonic oscillator: Reconciliation of the frequency-resolved frozen phonon multislice method with other theoretical approaches, Phys. Rev. B **108**, 094309 (2023).

[24] J. Barthel, P. M. Zeiger, J. Rusz, and L. J. Allen, Simple model for phonon spectroscopy using fast electrons, Phys. Rev. B **109**, 184105 (2024).

[25] J. Barthel and L. J. Allen, Interpretation of phonon spectroscopic data at atomic resolution in scanning transmission electron microscopy, Phys. Rev. B **110**, 094105 (2024).

[26] X. Yan, P. M. Zeiger, Y. Huang, H. Sun, J. Li, C. A. Gadre, H. Yang, R. He, T. Aoki, Z. Zhong *et al.*, Real-space visualization of frequency-dependent anisotropy of atomic vibrations, arXiv:2312.01694v1.

[27] X. Yan, P. M. Zeiger, Y. Huang, R. Wu, J. Rusz, and X. Pan, Revealing frequency-dependent atomic vibrational anisotropies in a centrosymmetric lattice by monochromated electron microscopy, Microsc. Microanal. **30**, 1128 (2024).

[28] J. Cowley, *Diffraction Physics*, 3rd revised ed. (North Holland, Amsterdam, 1995).

[29] K. Trueblood, H.-B. Bürgi, H. Burzlaff, J. Dunitz, C. Gramaccioli, H. Schulz, U. Shmueli, and S. Abrahams, Atomic dispacement parameter nomenclature. Report of a subcommittee on atomic displacement parameter nomenclature, Acta Cryst. A **52**, 770 (1996).

[30] T. W. Josefsson and L. J. Allen, Diffraction and absorption of inelastically scattered electrons for K-shell ionization, Phys. Rev. B **53**, 2277 (1996).

[31] Y. A. Abramov, V. G. Tsirelson, V. E. Zavodnik, S. A. Ivanov, and I. D. Brown, The chemical bond and atomic displacements in $SrTiO_3$ from x-ray diffraction analysis, Acta Cryst. B **51**, 942 (1995).

[32] J. M. Cowley and A. F. Moodie, The scattering of electrons by atoms and crystals. I. A new theoretical approach, Acta Cryst. **10**, 609 (1957).

[33] J. M. LeBeau, S. D. Findlay, L. J. Allen, and S. Stemmer, Quantitative atomic resolution scanning transmission electron microscopy, Phys. Rev. Lett. **100**, 206101 (2008).

[34] C.-L. Jia, J. Barthel, F. Gunkel, R. Dittmann, S. Hoffmann-Eifert, L. Houben, M. Lentzen, and A. Thust, Atomic-scale measurement of structure and chemistry of a single-unit-cell layer of $LaAlO_3$ embedded in $SrTiO_3$, Microsc. Microanal. **19**, 310 (2013).

[35] L.-M. Peng, Anisotropic thermal vibrations and dynamical electron diffraction by crystals, Acta Cryst. A **53**, 663 (1997).

[36] A. Weickenmeier and H. Kohl, Computation of absorptive form factors for high-energy electron diffraction, Acta Cryst. A **47**, 590 (1991).

[37] J. Barthel, Dr. Probe: A software for high-resolution STEM image simulation, Ultramicroscopy **193**, 1 (2018).

[38] N. R. Lugg, M. J. Neish, S. D. Findlay, and L. J. Allen, Practical aspects of removing the effects of elastic and thermal diffuse scattering from spectroscopic data for single crystals, Microsc. Microanal. **20**, 1078 (2014).